Catalysis Science & Technology

PAPER

Cite this: *Catal. Sci. Technol.*, 2016, **6**, 6605

2D-HfS_2 as an efficient photocatalyst for water splitting

Deobrat Singh,[a] Sanjeev K. Gupta,*[b] Yogesh Sonvane,*[a] Ashok Kumar[c] and Rajeev Ahuja[d]

Received 30th May 2016,
Accepted 23rd June 2016

DOI: 10.1039/c6cy01172a

www.rsc.org/catalysis

Two dimensional monolayer nanostructures for water splitting solar photocatalysts are drawing more attention due to their extraordinary properties. Using first principles calculations we have systematically investigated the structural, electronic and vibrational properties of corresponding HfS_2 monolayers in both hexagonal (1H) and trigonal (1T) phases. The most stable adsorption configurations and adsorption energies are calculated. The adsorption energy of H_2O on the substrate is 646.53 kJ mol^{-1} for the 1H-phase and 621.65 kJ mol^{-1} for the 1T-phase of HfS_2. This shows that H_2O molecules have a stronger interaction with the HfS_2 substrate. The calculated redox potentials of H_2O splitting lie properly astride the valence and conduction bands, suggesting that the monolayers of 1H- and 1T-HfS_2 show the same characteristics as a photocatalyst for water splitting. Furthermore, we also calculated that the optical band gaps for the 1H and 1T phases of HfS_2 are 2.60 eV and 3.10 eV, respectively. We have also calculated Raman spectrum signatures of the monolayer 1H and 1T-phase of the in-plane vibrational mode of the Hf and S atoms (E_{1g}) and the out-of-plane vibrational mode of S atoms (A_{1g} and A_{2u}). Our work suggests that a lot more research and attention in this field is needed for the practical application of the material as visible light active photocatalysts.

Introduction

Energy storage and conversion plays the greatest role in the development of modern society. Our dependence on fossil fuels, which are a limited and finite energy resource, has triggered researchers to look for alternative options. Moreover, these fuels produce energy expulsion, and as the global population increases this causes environmental pollution and a change in climate. This situation leads us to look for renewable and natural energy sources as sustainable alternatives to the current use of limited fossil fuels.[1] To fulfill the increasing global energy demands, water and sunlight has to be utilized to produce hydrogen through electrochemical or photocatalytic processes.[1,2] Note that hydrogen is regarded as one of the most efficient energy carriers for storing and transporting energy.

The photocatalytic splitting of water provides a route for clean hydrogen fuel generation which has been proposed by Dahl *et al.*[3] and Maeda *et al.*[4] In the process of the electrochemical decomposition of water, there must be a 1.23 eV potential difference between the anode and cathode. But the energy of visible radiation is slightly higher than the potential difference. Therefore, a meaningful photocatalyst must have its electronic band positions that straddle the redox potentials *i.e.* hydrogen evolution reaction (HER) and oxygen evolution reaction (OER), and a bandgap less than ≈1.6 eV to efficiently utilize solar energy and split H_2O into H_2.[5] In the photocatalytic process, the photocatalyst materials absorb photons from sunlight to create electron–hole pairs in order to initiate redox reactions.[5–6]

The synthesis of materials as photocatalysts is categorized into three generational types. The first generation shows only ultraviolet absorption for metals; the second generation shows visible light absorption for metals; and the third generation shows extended visible light absorption for two-dimensional (2D) metals/non-metals.[2–4] The first generation have the significant disadvantage of a restricted photon absorption window towards UV light only, which indicates poor solar-to-hydrogen (STH) conversion efficiencies. The second generation photocatalysts have a high capacity to absorb photons of visible light, however, the efficiency is poor because of inefficient charge transfer kinetics, high recombination rate of photo-generated carriers, and instability in acidic/alkaline medium.[7–12] The first and second generations of

[a] *Advanced Material Lab, Department of Applied Physics, S.V. National Institute of Technology, Surat 395007, India. E-mail: yas@ashd.svnit.ac.in*
[b] *Computational Materials and Nanoscience Group, Department of Physics, St. Xavier's College, Ahmedabad 380009, India. E-mail: sanjeev.gupta@sxca.edu.in*
[c] *Centre for Physical Sciences, Central University of Punjab, Bathinda, 151001, India*
[d] *Department of Physics and Astronomy, Uppsala University, Box 516, 751 20, Uppsala, Sweden*

photocatalysts mostly consist of oxides, sulfides and nitrides of titanium, cadmium, tungsten and transition-metal-dichalcogenides (TMDs). The metal-based photocatalysts have toxic and corrosive behavior, therefore, they can only be used in the presence of co-catalysts of precious metals (Pt, Au, Ag *etc.*).[13] In order to overcome this problem, alternative elemental and compound photocatalysts have been explored *e.g.* red-P, alpha-sulfur and boron have been reported as potential photocatalysts by researchers,[14–16] the experimental realization of water splitting on a titanium oxide electrode has been demonstrated,[5,17,18] and theoretical investigations of layered transition metal dichalcogenides such as MoS_2, $MoSe_2$, and TaS_2 have led them to be considered as potential candidates to catalyze solar water splitting.[19–22] In addition, the theoretical study by Zhuang and Hennig predicted that the monolayer of group-III monochalcogenides have ideal band edges for solar water splitting.[23]

The remarkable progress of research in this area has drawn our attention to look for materials which consist of a few atomic layers thick, which are highly functional compared to their bulk counterparts. Note that two dimensional materials have abnormal structural, electronic and electro-optical properties.[24–26] In this paper, we have investigated the electronic, vibrational and photocatalytic properties of the hexagonal (1H) and trigonal (1T) phases of HfS_2 using first-principles calculations based on density functional theory (DFT). We determined the band position of edge energies on the standard hydrogen electrode (SHE) potential scale, and presented the relevance and suitability of the different phases as photocatalysts for water splitting in terms of the redox potentials of water.

Methodology

First-principles calculations were performed using the Quantum ESPRESSO package,[27] which uses plane-wave basis sets to expand the Kohn–Sham orbital. Local density approximation (LDA) within the Perdew–Wang (PW) parametrization, generalized gradient approximation (GGA) in Perdew–Burke–Ernzerhof (PBE) and hybrid functional HSE06 parameterization were used to treat the exchange-correlation functional[28] for fully self-consistent density functional theory (DFT) calculations.[29,30] We used a norm-conserving pseudopotential for Hf and S atoms that includes the scalar-relativistic effect.[31] The Kinetic energy cutoff of 60 Ry and 300 Ry was used for electronic wave functions and charge densities, respectively. The Monkhorst–Pack scheme for *k*-point sampling of the Brillouin zone was used with a $23 \times 23 \times 1$ grid. The convergence criteria for energy in the SCF cycles were chosen to be 10^{-10} Ry. The geometric structures were optimized by minimizing the forces on individual atoms with the criterion that the total force on each atom is below 10^{-3} eV Å^{-1}. In order to mimic the two-dimensional system, the supercell was used to simulate the isolated structures, and the distance between images was larger than 20 Å in the *z*-direction (perpendicular to the plane of HfS_2) to avoid image interactions.

The phonon dispersion was obtained on a finer *q*-mesh, *i.e.*, $3 \times 3 \times 1$ using density functional perturbation theory by applying the acoustic sum rule for $q \rightarrow 0$. All the optimized geometric structures presented in the paper were obtained with the help of XCrySDen software.[32] To ensure dynamical stability and to analyze Raman fingerprints of the single layer crystal structures of the two phases, namely 1H-HfS_2 and 1T-HfS_2, phonon frequencies along the whole Brillouin Zone (BZ) were computed using the perturbation method with the forces obtained from the Quantum Espresso package.

Results and discussion

a) Stability of structures

To determine the energy landscape for a transformation between 1H and 1T polymorphs, we consider different configurations obtained by displacing (or sliding) one of the X-atomic sub-lattice planes with respect to the M-atom layer of the structure. The calculated optimized structural parameters of the triatomic X–M–X layer with two phases (Fig. 1), namely the lattice constant and bond length between Hf–S and S–S, are shown in Table 1. The calculated lattice parameters are found to be in good agreement with previously reported values.[33–36] Our calculated lattice constants at the GGA-PBE level of theory are 3.54 Å and 3.65 Å for the 1H and 1T-phase respectively. LDA is found to underestimate lattice constants by a significant manner (a^{LDA} = 3.38 Å for the 1H-phase and a^{LDA} = 3.48 Å for the 1T-phase). Moreover, the band structure of both phases of HfS_2 allotropes was calculated using the hybrid functional HSE06. Using the hybrid functional, the band gap increases with respect to the PBE from 1.36 eV to 2.66 eV for the 1H-phase and from 1.49 eV to 3.12 eV for the 1T-phase of HfS_2, which can be compared to the previous G_0W_0 functionals results obtained by F. A. Rasmussen *et al.*,[37] of 2.63 eV (1H-phase) and 2.98 eV (1T-phase) for HfS_2.

In order to determine the dynamic stability of the two phases, phonon dispersion calculations were performed around the high symmetric points in Brillouin Zone (BZ) (Fig. 2). The unit cell of the 1H and 1T-phases of HfS_2 consists of three atoms which give a total of 9 frequency modes where 3 are acoustic branches and other 6 are optical branches. The 1T-phase of HfS_2 is globally stable since the global energy minimum exists, and all phonon frequencies are positive and lowest energy acoustic mode near Γ (M–Γ direction) is not linear. In the case of the 1H-phase of HfS_2, all the modes contain positive values of frequencies, except the transverse acoustic mode near the Γ-point. These modes have imaginary frequencies near the Γ-point up to 5 cm^{-1} due to the softening of phonons, where a strong dependence of the frequency of this mode on the computational parameters is also observed. Our HfS_2 structure has a triatomic S1–Hf–S2 layer in both cases. The left side S1-atom is the first S-atom and the right side S2-atom is the second S-atom. So those three dispersion modes of the acoustical

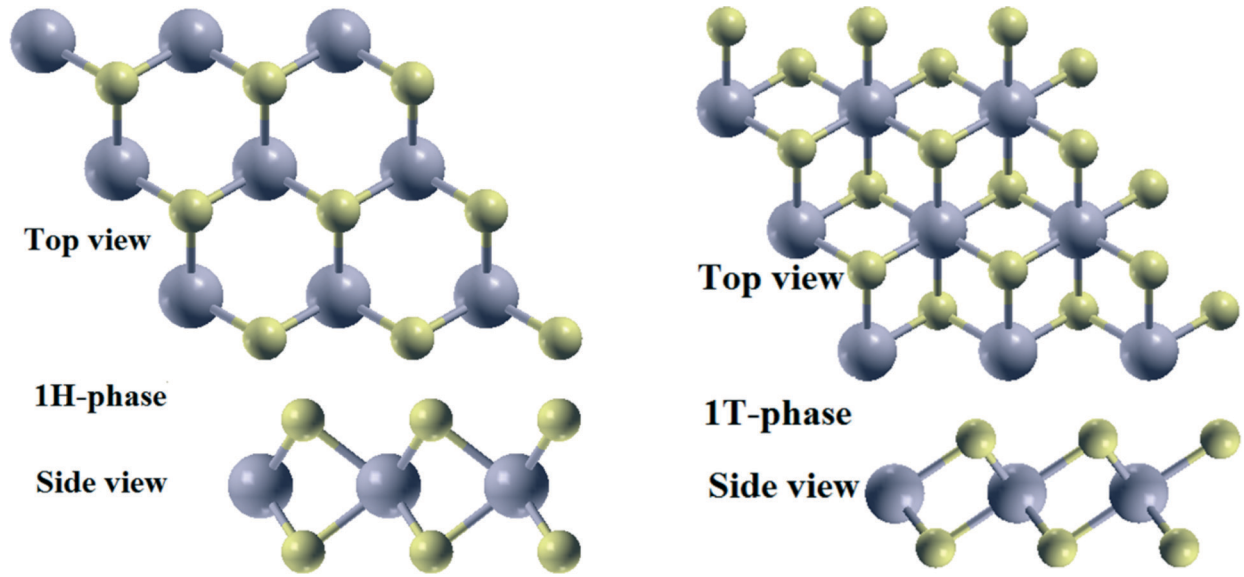

Fig. 1 The top view and side view of 1T and 1H-phases of HfS_2 with a 3 × 3 × 1 supercell.

Table 1 Comparison of structural parameters and band gap of 2D monolayer HfS_2 calculated by using different exchange correlation functionals along with other reported values

Properties	LDA	GGA	HSE06	Other
a (Å)	3.38 (1H),3.48 (1T)	3.54 (1H), 3.65 (1T)	3.539 (1H),3.651 (1T)	3.66,[34] 3.64[35,46] (1T)
D_{Hf-S} (Å)	2.52 (1H),2.50 (1T)	2.59 (1H), 2.58 (1T)	2.59 (1H), 2.57 (1T)	—
d_{S-S} (Å)	3.21 (1H),3.58 (1T)	3.21 (1H), 3.64 (1T)	3.17 (1H),3.61 (1T)	—
E_g (eV)	1.07 (1H),0.92 (1T)	1.36 (1H), 1.49 (1T)	2.66 (1H),3.12 (1T)	1.26,[34] 1.23[39] (1T)

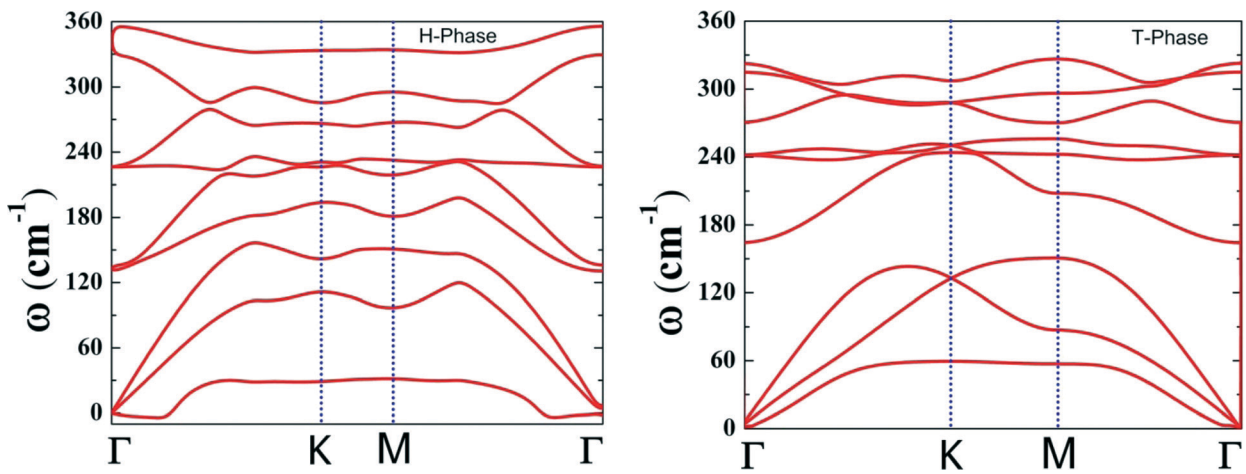

Fig. 2 Full phonon dispersion curve of monolayer 1H and 1T-phases of HfS_2.

branch can be easily distributed and are considered to be due to the heavier atom (Hf), while the upper 6 lines in the optical branch are considered due to the lighter atom (S).

We have performed calculations with a finer 3 × 3 × 1 q-mesh to improve the acoustic sum rule for $q \rightarrow 0$. The longitudinal acoustic (LA) branch in the direction Γ–K experiences a softening or downward bending to meet the first transverse acoustic branch (TA) at a degenerate point at K in the 1T-phase. In the Γ–M direction, Fig. 2 reveals an upward bending and both the LA and TA acoustical branch are degenerate in the 1T-phase. There is a relatively large splitting of bands along the Γ–M direction compared to the very small split in the Γ–K direction in the case of the 1T-phase. For the 1H-phase, all these acoustical and optical branches are degenerate. There is a softening of the TO mode corresponding to the second S-atoms along the Γ–M direction that

become degenerate with the LO corresponding to the first S-atom at the M-point. This downward bending can also be seen in the Γ–K direction (Fig. 2).

The separation between LO and TO branches in the Γ–M directions is very small. These branches belong to the second S-atom. The highest mode is at the centre of the BZ and its value is 326.5 cm^{-1} and 355.9 cm^{-1} for the 1T and 1H-phases, respectively.

Next we have investigated the Raman spectra of 1H and 1T-phases of HfS_2 (Fig. 3). We identify the Raman active modes which correspond to the same modes A at 233.54 cm^{-1}, 325.06 cm^{-1} and 361.62 cm^{-1} for the 1H-phase, while in the case of the 1T-phase, the Raman active modes are E_{1g}, A_{1g} and A_{2u} at 168.39 cm^{-1}, 293.12 cm^{-1} and 294.79 cm^{-1}, respectively, that correspond to the in-plane vibration of the Hf and S atoms (E_{1g}) and the out-of-plane vibration of S atoms (A_{1g} and A_{2u}) in the HfS_2 structure. The difference in peak position between the E_{1g}, A_{1g} and A_{2u} bands, which is a strong indicator of the number of layers, was approximately 124.73 and 1.67 cm^{-1} for the 1T-phase, respectively, and in the case of the 1H-phase, the differences between positions are 91.51 and 36.57 cm^{-1} for the same Raman active modes (A), respectively.

b) Electronic structure

The electronic configuration of Hf is [Xe] $4f^{14}$ $5d^2$ $6s^2$ and S has an electronic configuration of [Ne] $3s^2$ $3p^4$. The f-orbitals of the Hf atom are completely filled, but Hf has 2 unpaired 5d electrons and S has 2 unpaired 3p electrons. As S (2.58) is more electronegative than Hf (1.30),[38] the S atom attracts electrons from the Hf atom. Basically, Hf is a transition metal; all the outer most orbital electrons freely move up to the Fermi levels. The electronic band structures of two dimensional monolayer structures of 1H-HfS_2 (Fig. 4) and 1T-HfS_2 (Fig. 5) clearly show semiconducting nature, with indirect band gaps of 2.66 eV and 3.12 eV, respectively. The direct band gap at the M-point (2.96 eV) is slightly larger than the indirect band gap for the 1H-phase, but in case of the 1T-phase, the direct band gap of 4.22 eV is significantly larger than the indirect band gap value. The detailed comparison of band gap values using different correlation functionals is tabulated in Table 1.

We now examine the projected density of states (PDOS) to study the orbital contribution to valence and conduction bands. The S-3p contribution of the energy band near the Fermi level is more dominant compared to the Hf-5d orbital in the valance band region, while in the conduction band region near the Fermi energy, most of the contribution is observed to be due to the Hf-5d orbitals (Fig. 4 and 5). The electronic distributions are also spatially correlated to the atomic structure. The conduction-band states at the M-point are mainly due to localized d orbitals on the Hf atoms, located in the middle of the S–Hf–S layered structure and relatively unaffected by interlayer coupling. However, the states near the Γ-point are due to combinations of the antibonding P_z-orbitals on the S atoms and the d orbitals on Hf atoms, and have a strong interlayer coupling effect.

c) Hafnium disulphide as a water splitting photocatalyst

We determined band edge energies and aligned them on the standard hydrogen electrode (SHE) potential scale. Based on these, we discuss their positions relative to the redox potentials of water splitting using different exchange correlation energy functionals. The reactivity of a catalyst is determined by its work function (φ), which is defined as the minimum amount of work required to remove an electron from the interior of a solid to the vacuum level and is given by

$$\text{Work function } (\varphi) = E_{\text{vacuum}} - E_{\text{F}}(\text{or } E_{\text{VBM}}) \quad (1)$$

where E_{F} is the Fermi energy and E_{VBM} is the energy of the valence band maximum.

The macroscopic planar average of the electronic potential of monolayer 1H- and 1T-HfS_2 obtained as a function of Z (perpendicular to its plane) is presented in Fig. 6. The value of the work function (φ) has been estimated as 6.56 eV and

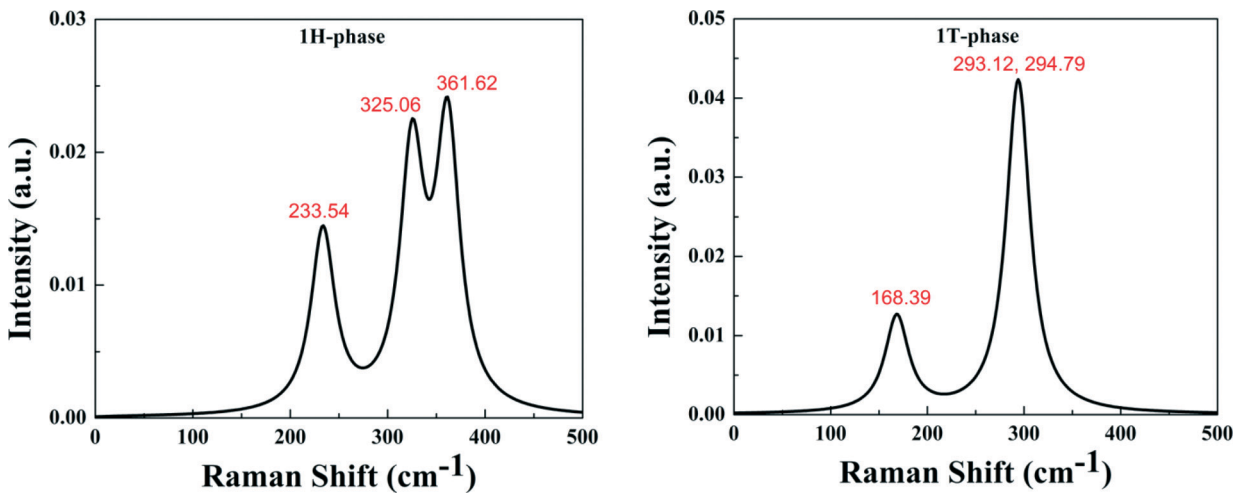

Fig. 3 The Raman spectra of 1H and 1T-HfS_2 monolayer before the photocatalytic hydrogen reaction.

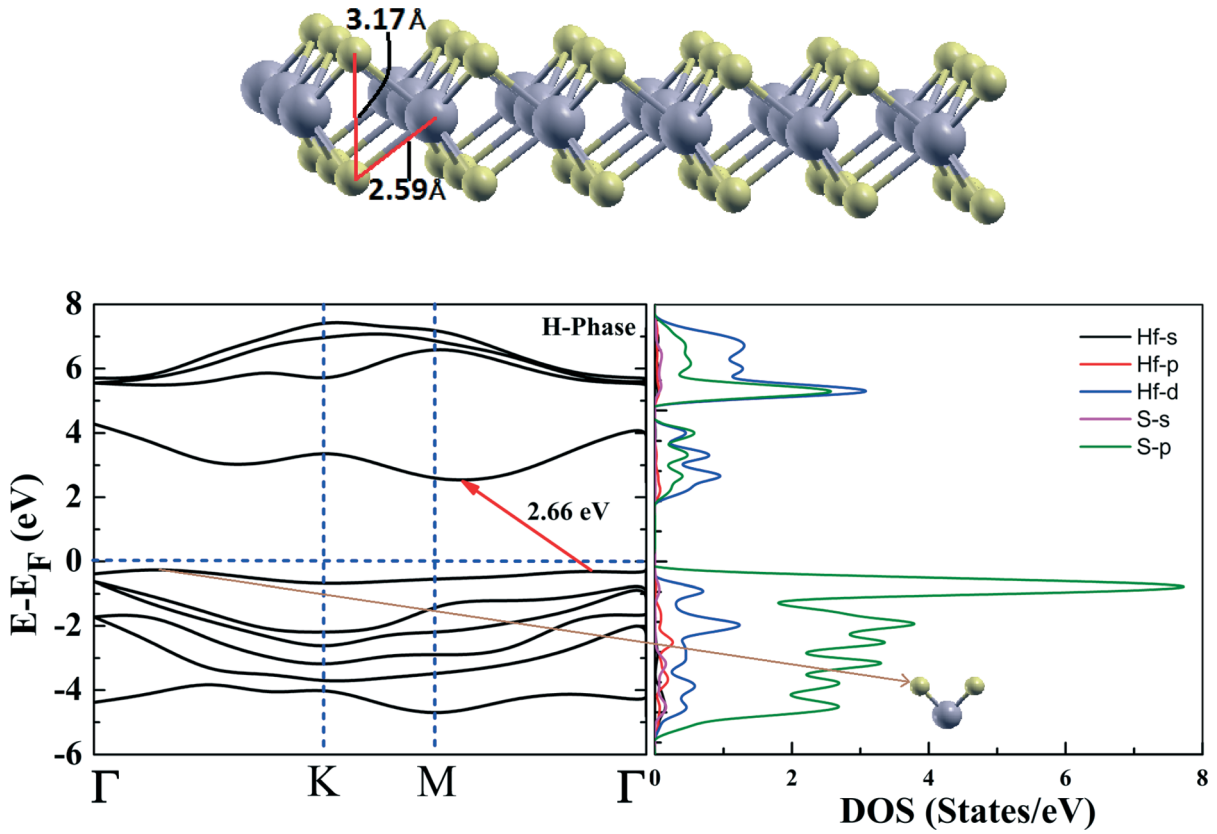

Fig. 4 Optimized geometric structure, electronic band structure and partial density of states (PDOS) of the 1H-phase of HfS_2. The inserted molecule of HfS_2 shows the p-orbital contribution of S atom in the VBM.

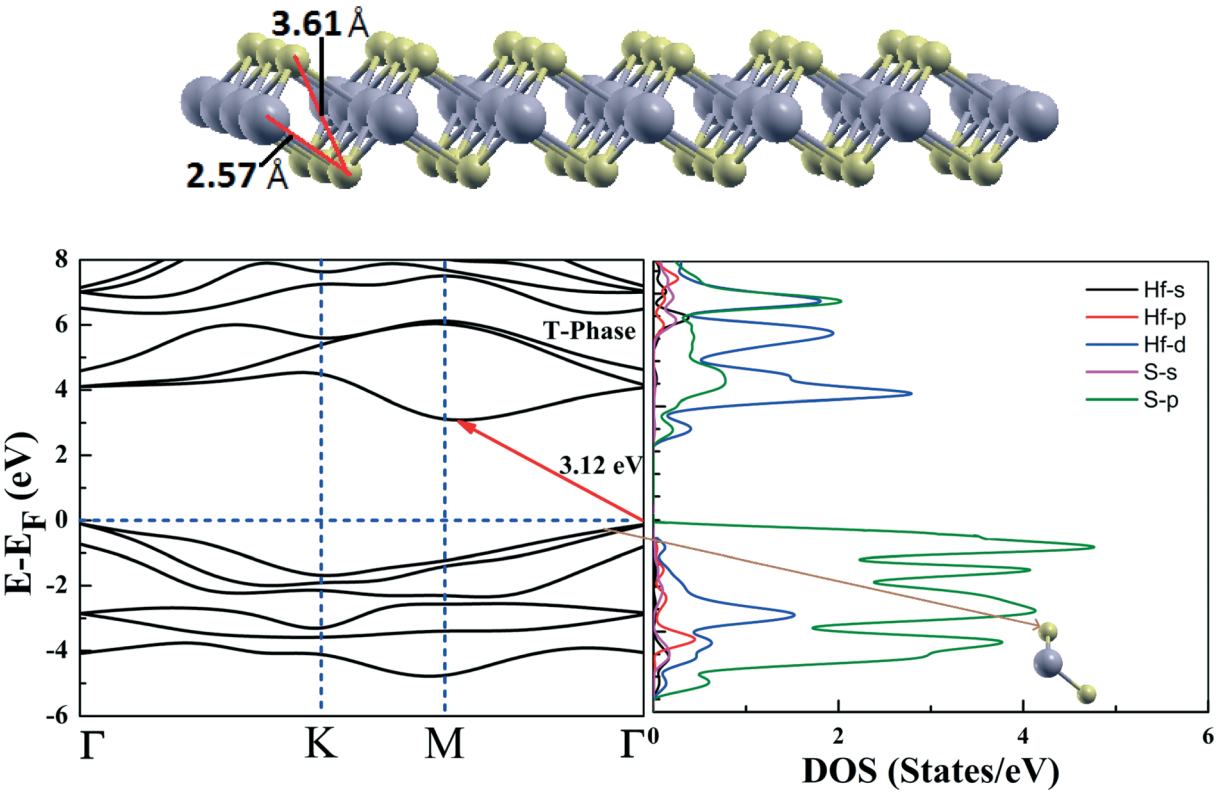

Fig. 5 Optimized geometric structure, electronic band structure and partial density of states (PDOS) of the 1T-phase of HfS_2. The inserted molecule of HfS_2 shows the p-orbital contribution of S atom in the VBM.

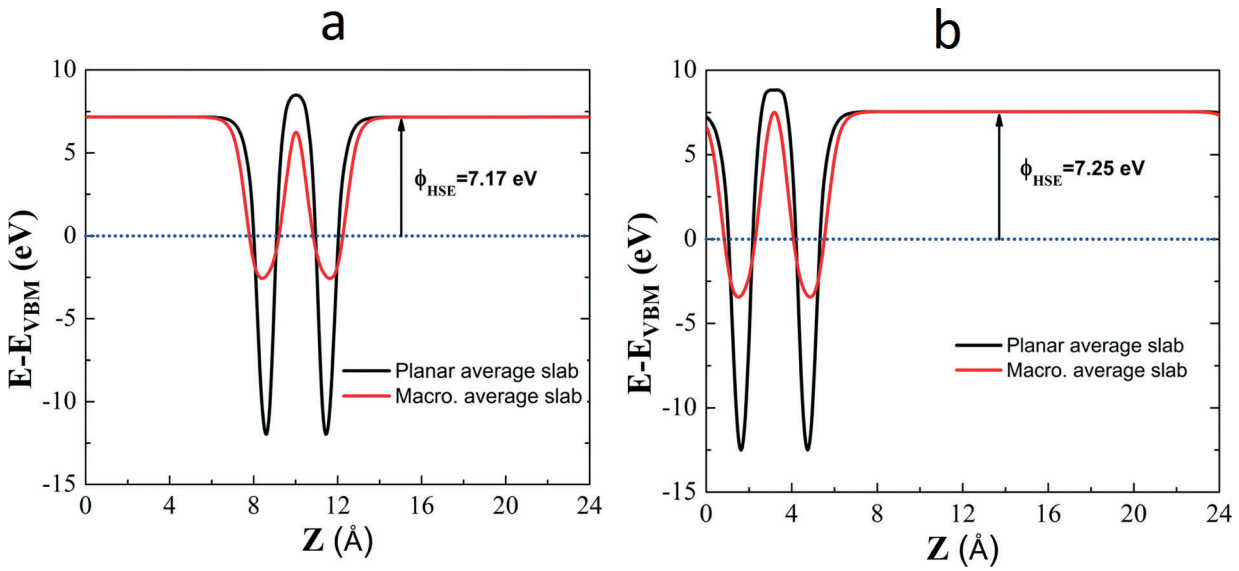

Fig. 6 (a) Work function of the 1H-phase of HfS_2 and (b) work function of the 1T-phase of HfS_2.

5.92 eV for 1H-phase and 6.42 eV and 6.25 eV for the 1T-phase with GGA and LDA, respectively. Moreover, the work function of both phases of HfS_2 allotropes was calculated using the hybrid functional HSE06. Using the hybrid functional, the work function increases from 6.56 eV to 7.17 eV for the 1H-phase and from 6.42 eV to 7.25 eV for the 1T-phase of HfS_2. Our calculated values are comparable with the previously reported work function of 6.21 eV for 1T-HfS_2.[39] These are also comparable with the work function of other compounds such as GaS (6.72 eV), Ga^{2+} compounds, and CdS (7.12 eV), indicating that both phases of HfS_2 have a better catalytic activity than GaS[40] and CdS.[41] CdS is a better catalyst for water splitting and from the reported values of CdS we compare our work function values, which may indicate a better catalyst for water splitting. Note that for a photocatalyst, the work function is inversely proportional to the catalytic activity.

Analyzing the valence and conduction bands position (aligned) on the standard hydrogen electrode (SHE) potential scale,[37,42–46] we found that the redox potentials for H_2O splitting lay properly astride the valence and conduction bands, suggesting that the monolayers of 1H and 1T-HfS_2 could be potential candidates as water splitting photocatalysts (Fig. 7).

The band alignment of HfS_2 with respect to the standard hydrogen electrode (SHE) reveals that the valence band maximum (VBM) of the 1H-phase of HfS_2 is not more negative than that of the redox potential of O_2/H_2O (+1.23 eV *vs.* vacuum) while in the case of the 1T-phase of HfS_2, the VBM is less negative in LDA, GGA and HSE06 calculations. However, its conduction band minimum (CBM) is more negative than that of the H^+/H_2 reduction potential (0.0 eV *vs.* vacuum) in the LDA calculation of the 1H-phase, whereas in the GGA and HSE06 calculations show less negative value for the same phase, while in the 1T-phase, the CBM is also negative in all of them calculations, thereby suggesting that both phases of HfS_2 are capable for water splitting. Note that at ambient conditions, the CBM of phosphorene was reported to be more negative than the redox potential of H^+/H_2 while the VBM is not more positive than the redox potential of O_2/H_2O, which suggests that phosphorene is suitable for water splitting under vacuum conditions.[47]

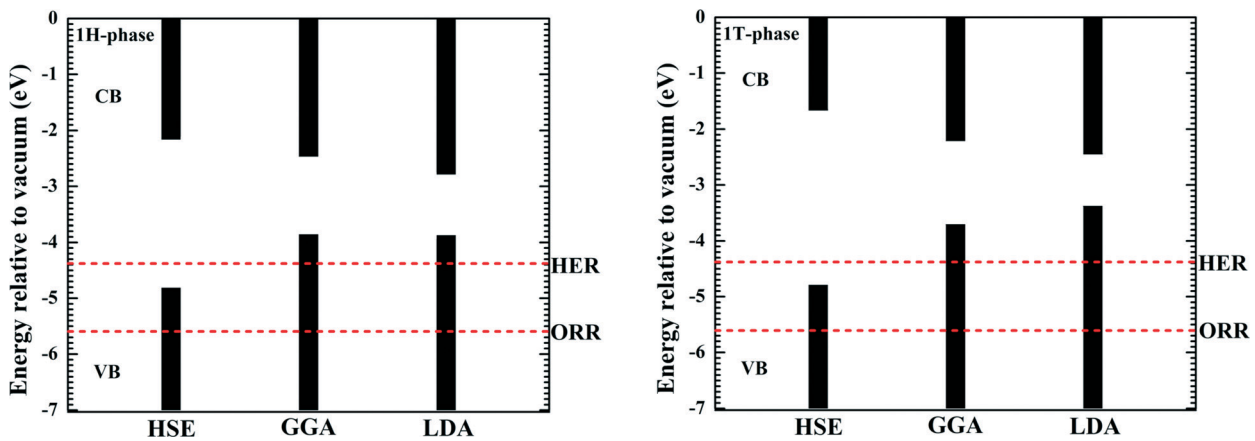

Fig. 7 Band positions of monolayer 1H and 1T-phases of HfS_2 using LDA, GGA and HSE06 functionals.

We have calculated the optical absorption spectra of HfS_2.[48] HfS_2 is found to exhibit a strong absorption spectrum, mainly in the visible region and the ultraviolet region. Our calculations show that the optical band gaps for the 1H and 1T phases of HfS_2 are 2.60 eV and 3.10 eV, respectively, in the low energy zone (Fig. 8).

For verification of the potential of monolayers of the two phases (1H and 1T) of HfS_2 as photocatalysts, we investigated the adsorption of H_2O molecules at various coverages on the (3 × 3 × 1) surface of HfS_2. All the coverages were calculated by considering only the top two atomic layers of monolayer HfS_2. Water molecules were initially placed at a distance of ≈1.4 Å from the HfS_2 substrate. At this distance, water molecules feel a repulsive force so that they drift away from the substrate to distances ≈3.19 Å. The configurations with 1 to 8 water (H_2O) molecules adsorbed onto the outer surface of the monolayer have been considered.

In the structural relaxation of water molecules adsorbed onto the monolayer structures of both phases of HfS_2, the unit cell volume and shape were kept fixed, while the Hf and S atoms close to the adsorbate were allowed to change. Inspection of the optimized structures of freezing the Hf and S atoms and test calculations where the whole atoms are allowed to relax shows that freezing the partial atoms does not have a significant effect on the results. Therefore, while relaxing the adsorption configurations of the HfS_2 monolayer structure, all the positions of the atoms are allowed to change. The adsorption energy is defined as:

$$E_{\text{ad.}} = \frac{E_{(H_2O+HfS_2)} - E_{HfS_2} - nE_{H_2O}}{n} \quad (2)$$

where $E_{(H_2O+HfS_2)}$ denotes the total energy of the optimized adsorption configuration, E_{HfS_2} and E_{H_2O} are the energies of the monolayer HfS_2 substrate and isolated water molecules, respectively, and n is the total number of H_2O molecules. A negative value of E_{ad} indicates exothermic and energetically favorable adsorption. We found that the intermediate adsorption energy of H_2O is 646.52 kJ mol^{-1} and 610.4 kJ mol^{-1} for the 1H- and 1T-phases of HfS_2 respectively. The adsorption energy of H_2O on the substrate is 646.53 kJ mol^{-1} for the 1H-phase and 621.65 kJ mol^{-1} for the 1T-phase of HfS_2. This shows that H_2O molecules have a stronger interaction with the HfS_2 substrate but according to S. Kouser, *et al.*,[40] the material GaS showed a less strong interaction between substrate and water molecules compared to HfS_2.

The contribution of interaction energy between the H_2O molecules in the complex (substrate + H_2O) can be determined by freezing them in their adsorbed positions and removing the substrate. The interaction energy of H_2O molecules $E_{int}^{H_2O}$ is calculated as:

$$E_{int}^{H_2O} = \frac{E_{nH_2O} - nE_{H_2O}}{n} \quad (3)$$

where E_{nH_2O} and E_{H_2O} are the total energies of n fixed H_2O molecules without substrate and an isolated H_2O molecule, respectively. We obtained the intermolecular interaction energies as 623.03 kJ mol^{-1} (1H) and 618.59 kJ mol^{-1} (1T).

Next, we studied the different coverages of H_2O (0.98–7.84 mmol g^{-1}, where n = 1 to 8 per 3 × 3 × 1 supercell) on monolayer HfS_2. At a low coverage (0.98 mmol g^{-1}), we get interactions [E_A = 201.25 kJ mol^{-1} (1H) and E_A = 621.65 kJ mol^{-1} (1T)] between H_2O molecules and the HfS_2 substrate, purely due to van der Waal forces. As the concentration increases, the adsorption energy varies randomly in the range of 80.43 to 646.52 kJ mol^{-1} for the 1H-phase and in the case of the 1T-phase there is a slight decrement in the adsorption energy in the range of 607.60 to 621.65 kJ mol^{-1}, as shown in Fig. 9. We have also taken a 5 × 5 × 1 supercell in both cases (1H and 1T-phase), giving the adsorption energy as 21.335 kJ mol^{-1} and 0.845 kJ mol^{-1} and the interaction energy as 323.591 kJ mol^{-1} and 309.496 kJ mol^{-1}, respectively, which is quite large, due to the fact that the system has not got perfect global minima, so we have not discussed this more in detail.

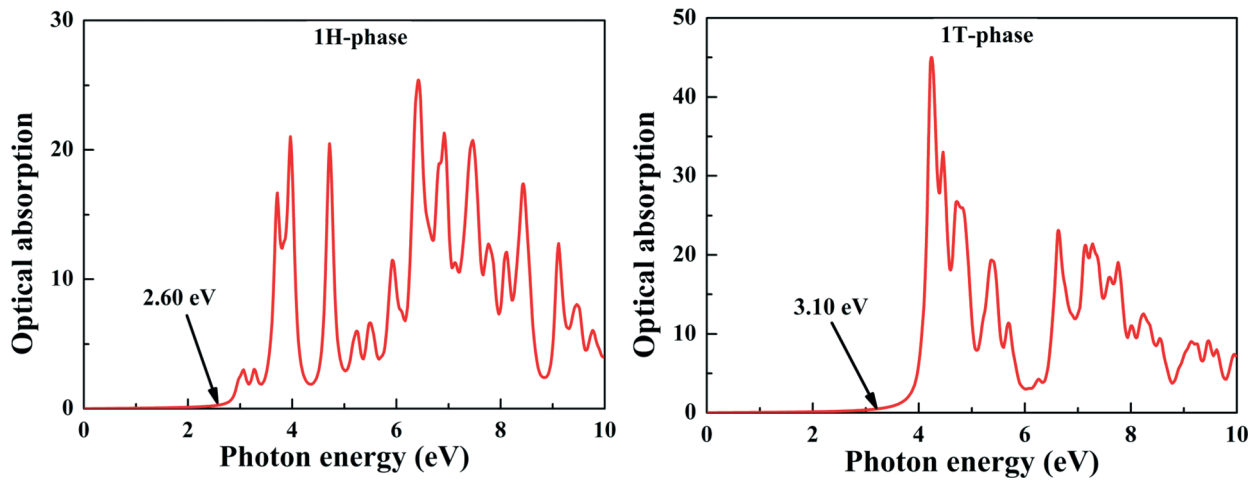

Fig. 8 Optical absorption spectra for both phases (1H and1T) of HfS_2.

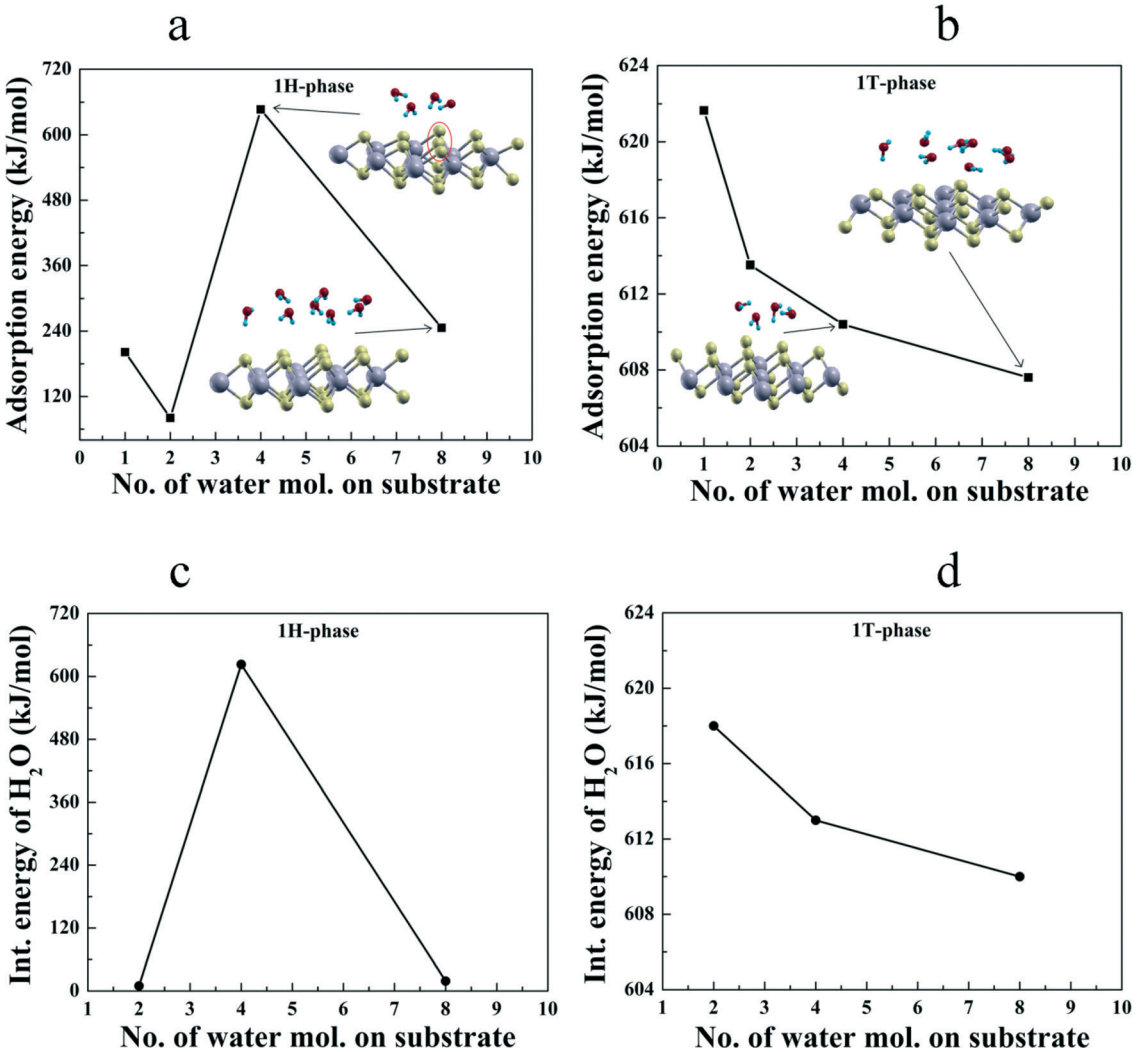

Fig. 9 Adsorption energy (a and b) as a function of different coverages of H_2O molecules on 3 × 3 × 1 substrates of both phases (1H and 1T) of HfS_2, and (c) and (d) represent the interaction energy of the water molecule *vs.* no. of water molecules on the substrate in both phases.

To understand such anomalous adsorptive behavior, we have separated the intermolecular interaction energy from that of the H_2O molecules with the substrate ($E_A^{'}$) and the H_2O molecules themselves ($E_{int}^{H_2O}$), where $\left(E_A^{'}\right)$ [39] is calculated as:

$$E_A^{'} = E_A - E_{int}^{H_2O} \quad (4)$$

Positive values of adsorption energy indicate the dissociation of H_2O molecules.

Photocatalytic water splitting decomposes water into hydrogen and oxygen in the presence of a semiconductor material that can absorb photons when irradiated by sunlight. This is the nub of the whole photocatalytic process and can be demonstrated as:[49]

$$H_2O = \frac{1}{2}O_2 + H_2;\ \Delta G = +237\ \text{kJ mol}^{-1} \quad (5)$$

The photocatalytic water splitting reaction is an 'uphill' reaction that involves a significant change in Gibbs energy, ΔG (+237 kJ mol^{-1}). Therefore, the minimum energy required by the photocatalyst from the stand point of thermodynamics is 1.23 eV, which is given by:

$$E^0 = \left|-\frac{\Delta G}{nF}\right| \quad (6)$$

where E^0 is the electrode potential, n is the number of electrons per mole of product (2 in this instance) and F is the Faraday constant in C mol^{-1}. However, when energy losses due to the overpotential are counted, the practical minimum energy band gap rises to approach 2.03 eV. Moreover, not all material with a band gap greater than 1.23 eV can be used as a water splitting photocatalyst.[24] According to the standard hydrogen electrode (SHE), the respective conduction band minimum of the material must lie at a more negative potential than the reduction potential (H^+/H_2: 0.0 eV *vs.* vacuum) and

the valence band maximum must exhibit a more positive potential than the oxidation potential (O_2/H_2O: +1.23 eV *vs.* vacuum) of water,[50–53] as shown in Fig. 6.

When the energy of an irradiated photon is equal to or greater than the intrinsic band gap of the photocatalyst material, an electron from the valence band will be excited to the conduction band, leaving behind a hole in the valence band. These photogenerated carriers have a general tendency to radiatively combine and annihilate each other. If the electron–hole pair can survive the recombination, it will reach the surface of the photocatalyst where it will react to adsorb molecules and initiate water reduction and oxidation reactions.[24]

Conclusion

We studied photocatalytic semiconductors, and plotted their band position alignment relative to the valence and conduction band edges as well as the water redox potentials. According to these potentials, our systems are energetically and dynamically stable. On the other hand, many non-oxides are resistant to electron reduction, and therefore may be used as a p-type photocathode provided that the total oxidation is prevented in the working devices. The method we used is universal and can be applied to evaluate the stability of any semiconductor. The most stable adsorption configurations and adsorption energies are calculated and the H_2O molecule has a higher interaction with the HfS_2 substrate. The maximum adsorption energy of H_2O on the substrate is 646.53 kJ mol^{-1} for the 1H-phase and 621.65 kJ mol^{-1} for the 1T-phase of HfS_2. HfS_2 was found to exhibit a strong absorption spectrum, mainly in the visible region and ultraviolet region. Our calculations show that the optical band gaps for the 1H and 1T phases of HfS_2 are 2.60 eV and 3.10 eV, respectively, in the low energy zone. We believe that our presented work will be useful in guiding the search for stable photocathode materials.

Acknowledgements

S. K. G. acknowledges the use of high performance computing clusters at IUAC, New Delhi and YUVA, PARAM, Pune to obtain the partial results presented in this paper. SKG also thank the Science and Engineering Research Board (SERB), India for the financial support (Grant no.: YSS/2015/001269).

References

1 B. A. Pinaud, J. D. Benck, L. C. Seitz, A. J. Forman, Z. Chen, T. G. Deutsch, B. D. James, K. N. Baum, G. N. Baum, S. Ardo, H. Wang, E. Miller and T. F. Jaramillo, *Energy Environ. Sci.*, 2013, **6**, 1983–2002.
2 D. Gust, T. A. Moore and A. L. Moore, *Acc. Chem. Res.*, 2009, **42**, 1890–1898.
3 S. Dahl and I. Chorkendorff, *Nat. Mater.*, 2012, **11**, 100–101.
4 K. Maeda, K. Teramura, D. Lu, T. Takata, N. Saito, Y. Inoue and K. Domen, *Nature*, 2006, **440**, 295–295.
5 K. H. A. Fujishma, *Nature*, 1972, **232**, 37.
6 K. Maeda, K. Teramura, D. Lu, T. Takata, N. Saito, Y. Inoue and K. Domen, *Nature*, 2006, **440**, 295–295.
7 Y. Tachibana, L. Vayssieres and J. R. Durrant, *Nat. Photonics*, 2012, **6**, 511–518.
8 F. Zuo, L. Wang, T. Wu, Z. Zhang, D. Borchardt and P. Feng, *J. Am. Chem. Soc.*, 2010, **132**, 11856–11857.
9 R. Asahi, T. Morikawa, T. Ohwaki, K. Aoki and Y. Taga, *Science*, 2001, **293**, 269–271.
10 X. Li, N. Kikugawa and J. Ye, *Adv. Mater.*, 2008, **20**, 3816–3819.
11 C. Z. Wen, Q. H. Hu, Y. N. Guo, X. Q. Gong, S. Z. Qiao and H. G. Yang, *Chem. Commun.*, 2011, **47**, 6138–6140.
12 Q. Li, H. Meng, P. Zhou, Y. Zheng, J. Wang, J. Yu and J. Gong, *ACS Catal.*, 2013, **3**, 882–889.
13 Y. Zheng, Y. Jiao, Y. Zhu, L. H. Li, Y. Han, Y. Chen, A. Du, M. Jaroniec and S. Z. Qiao, *Nat. Commun.*, 2014, **5**, 3783.
14 F. Wang, W. K. H. Ng, J. C. Yu, H. Zhu, C. Li, L. Zhang, Z. Liu and Q. Li, *Appl. Catal., B*, 2012, **111–112**, 409–414.
15 G. Liu, P. Niu, L. Yin and H.-M. Cheng, *J. Am. Chem. Soc.*, 2012, **134**, 9070–9073.
16 G. Liu, L.-C. Yin, P. Niu, W. Jiao and H.-M. Cheng, *Angew. Chem., Int. Ed.*, 2013, **52**, 6242–6245.
17 H. Kazuhito, I. Hiroshi and F. Akira, *Jpn. J. Appl. Phys.*, 2005, **44**, 8269.
18 A. Kudo and Y. Miseki, *Chem. Soc. Rev.*, 2009, **38**, 253–278.
19 U. Maitra, U. Gupta, M. De, R. Datta, A. Govindaraj and C. N. R. Rao, *Angew. Chem., Int. Ed.*, 2013, **52**, 13057.
20 U. Maitra, S. R. Lingampalli and C. N. R. Rao, *Curr. Sci.*, 2014, **106**, 518.
21 U. Gupta, B. S. Naidu, U. Maitra, A. Singh, S. N. Shirodkar, U. V. Waghmare and C. N. R. Rao, *APL Mater.*, 2014, **2**, 092802.
22 U. Gupta, B. G. Rao, U. Maitra, B. E. Prasad and C. N. R. Rao, *Chem. – Asian J.*, 2014, **9**, 1311.
23 H. L. Zhuang and R. G. Hennig, *Chem. Mater.*, 2013, **25**, 3232.
24 M. Z. Rahman, P. Kwong, K. Davey and S. Qiao, *Energy Environ. Sci.*, 2016, **9**, 709–728.
25 L. E. Conroy and K. C. Park, *Inorg. Chem.*, 1968, **7**(3), 459–463.
26 A. Cingolani, *et al.*, *Solid State Commun.*, 1987, **62**(2), 121–123.
27 P. Giannozzi, *et al.*, Quantum Espresso: a modular and open-source software project for quantum simulations of materials, *J. Phys.: Condens. Matter*, 2009, **21**, 395502.
28 J. P. Perdew, K. Burke and M. Ernzerhof, Generalized gradient approximation made simple, *Phys. Rev. Lett.*, 1996, **77**, 3865.
29 P. Hohenberg and W. Kohn, Inhomogeneous Electron Gas, *Phys. Rev.*, 1964, **136**, B864.
30 W. Kohn and L. J. Sham, *Phys. Rev.*, 1965, **140**, A-1133.
31 www.quantum-espresso.org/pseudopotentials.
32 A. Kokalj, *Comput. Mater. Sci.*, 2003, **28**, 155, Code available from http://www.xcrysden.org.
33 Jun Kang, Hasan Sahin and F. M. Peeters, *Phys. Chem. Chem. Phys.*, 2015, **17**(41), 27742–27749.
34 David M. Guzman and A. Strachan, *J. Appl. Phys.*, 2014, **115**(24), 243701.

35 H. Guo, N. Lu, L. Wang, X. Wu and X. C. Zeng, *J. Phys. Chem. C*, 2014, **118**(13), 7242–7249.
36 C. Gong, *et al.*, *Appl. Phys. Lett.*, 2013, **103**(5), 053513.
37 F. A. Rasmussen and K. S. Thygesen, *J. Phys. Chem. C*, 2015, **119**(23), 13169–13183.
38 L. Pauling, *J. Am. Chem. Soc.*, 1947, **69**(3), 542–553.
39 C. Gong, H. Zhang, W. Wang, L. Colombo, R. M. Wallace and K. Cho, *Appl. Phys. Lett.*, 2013, **103**(5), 053513.
40 S. Kouser, A. Thannikoth, U. Gupta, U. V. Waghmare and C. N. R. Rao, *Small*, 2015, **11**(36), 4723–4730.
41 J. L. Freeouf and J. M. Woodall, *Appl. Phys. Lett.*, 1981, **39**(9), 727–729.
42 V. Stevanović, S. Lany, D. S. Ginley, W. Tumas and A. Zunger, *Phys. Chem. Chem. Phys.*, 2014, **16**(8), 3706–3714.
43 W. A. Smith, I. D. Sharp, N. C. Strandwitz and J. Bisquert, *Energy Environ. Sci.*, 2015, **8**(10), 2851–2862.
44 W. J. Chun, A. Ishikawa, H. Fujisawa, T. Takata, J. N. Kondo, M. Hara and K. Domen, *J. Phys. Chem. B*, 2003, **107**(8), 1798–1803.
45 A. K. Singh, K. Mathew, H. L. Zhuang and R. G. Hennig, *J. Phys. Chem. Lett.*, 2015, **6**(6), 1087–1098.
46 H. L. Zhuang and R. G. Hennig, *J. Phys. Chem. C*, 2013, **117**(40), 20440–20445.
47 B. Sa, Y.-L. Li, J. Qi, R. Ahuja and Z. Sun, *J. Phys. Chem. C*, 2014, **118**, 26560–26568.
48 J. Qiao, X. Kong, Z.-X. Hu, F. Yang and W. Ji, *Nat. Commun.*, 2014, **5**, 4475.
49 Graeme Henkelman, A. Arnaldsson and H. Jónsson, *Comput. Mater. Sci.*, 2006, **36**(3), 354–360.
50 M. Z. Rahman, P. Kwong, K. Davey and S. Qiao, *Energy Environ. Sci.*, 2016, **9**, 1513–1514.
51 M. G. Walter, E. L. Warren, J. R. McKone, S. W. Boettcher, Q. Mi, E. A. Santori and N. S. Lewis, *Chem. Rev.*, 2010, **110**, 6446–6473.
52 Y. Tachibana, L. Vayssieres and J. R. Durrant, *Nat. Photonics*, 2012, **6**, 511–518.
53 Y. Jiao, Y. Zheng, M. Jaroniec and S. Z. Qiao, *Chem. Soc. Rev.*, 2015, **44**, 2060–2086.

